**Showcasing research from Pohang University of Science and Technology, South Korea.**

Analytic bond order potential for indium gallium zinc oxide

The first parameterization of the bond order potential for InGaZnO$_4$ compounds showcases exceptional accuracy in predicting their structures. By employing this advanced potential, simulations of thin film deposition enable the identification of optimal process conditions, highlighting the significance of low deposition rates and sputtering targets with high oxygen content.
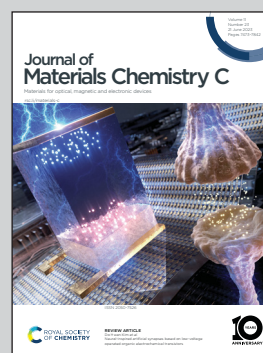
ROYAL SOCIETY
OF **CHEMISTRY**

rsc.li/materials-c

PAPER

Analytic bond order potential for indium gallium zinc oxide

Yun Ho Lee, Su Hyun Park and Byoung Don Kong ⓘ *

We report the analytic bond order potential (ABOP) parameters for the molecular dynamics of the indium gallium zinc oxide (IGZO) quarterly compounds. The potential parameters were developed based on first principles calculations and adjusted to follow the experimental observations. Through the phase transition simulation from crystalline to amorphous by the melt-quenching method, the developed potential is in excellent agreement with the experimental observations in the average bond lengths and density changes (from 5.91 g cm^{-3} to 5.69 g cm^{-3}) along with good stability at room temperature. To demonstrate the broad applicability of the developed potential, thin film formation by sputtering was simulated. An amorphous phase film of In : Ga : Zn = 1 : 0.93 : 0.58 was successfully reproduced with the sputtering target of InGaZnO$_4$ under room temperature conditions, which shows good agreement with the experimental results. To find an ideal target composition for the film with few oxygen vacancies, which can induce the negative bias stress, multiple sputtering simulations were performed. The results suggest that the sputtering targets must contain six times higher oxygen contents than the metal components.

Introduction

Indium gallium zinc oxide (IGZO) compounds are crucial wide bandgap materials due to their outstanding properties, such as high mobility, low leakage current, and favourable low-temperature process conditions.[1–4] These characteristics make amorphous InGaZnO$_4$ (a-IGZO) an excellent alternative to amorphous silicon (a-Si)[5,6] of thin film transistors (TFTs) in display applications, and researchers are actively exploring its potential in memory[7,8] and logic[9,10] devices. In particular, IGZO has the potential to be a promising candidate for 3D NAND flash memory devices where an a-Si channel is used. However, IGZO compounds have complex structures, and their physical properties are not fully understood. IGZO compounds are quarterly materials with various stable phases. Indium and oxygen form an octahedral geometry, while gallium and zinc form a tetrahedral bond with oxygens.[11] The octahedrons and tetrahedrons can be connected through oxygen at various angles, resulting in numerous possible atomic configurations with significant changes in its electrical properties. For instance, the carrier mobility can vary up to seven times from 10 cm^2 V^{-1} s^{-1} to 70 cm^2 V$^-$ s^{-1}[12] due to changes in chemical compositions[13,14] or the phase change from amorphous to crystalline.[14,15] Various studies have attempted to predict the diverse phases and analytically determined defect states, such as oxygen vacancies and local disorders of IGZO using density

Department of Electrical Engineering, Pohang University of Science and Technology (POSTECH), Pohang 37673, Korea. E-mail: bdkong@postech.ac.kr

functional theory (DFT).[16–18] While DFT has proven to be a powerful tool for understanding the electronic structure and properties of materials, it does have some limitations. DFT calculations are typically limited to small-scale systems consisting of only a few tens of atoms due to the computational demands of accounting for all electron interactions. Additionally, DFT is primarily used to obtain ground-state energies and properties, so applying it to dynamic processes like film formation through sputtering requires extra effort and extensive computations.

Molecular dynamics (MD) simulations are ideal for studying such mesoscopic scale variations. However, using general two-body potentials, which have been only available for IGZO so far, oversimplifies the system, describing the interactions between the atoms only by distances. This treats a crystal as fluid and the complex interactions present in crystals, such as covalent and ionic bonds, are not represented properly.[19,20] As such, simple two-body potentials often lead to unsatisfactory results in MD simulations. For example, in a study of the conduction paths of electrons in IGZO structures, Orita *et al.*[21] used the Buckingham potential, but had to fix the simulation volume with the known lattice constant to generate reasonable structures. This additional treatment limits the versatility of the MD simulations and makes it challenging to apply the potential under various pressure and temperature conditions, thereby compromising the accuracy and generalizability of the results.

To address these limitations, the bond order potential (BOP) was proposed, with the Tersoff potential being the most well-known example. As shown in Fig. 1b, the Tersoff potential introduces a dependence on the local bond order into the

This journal is © The Royal Society of Chemistry 2023

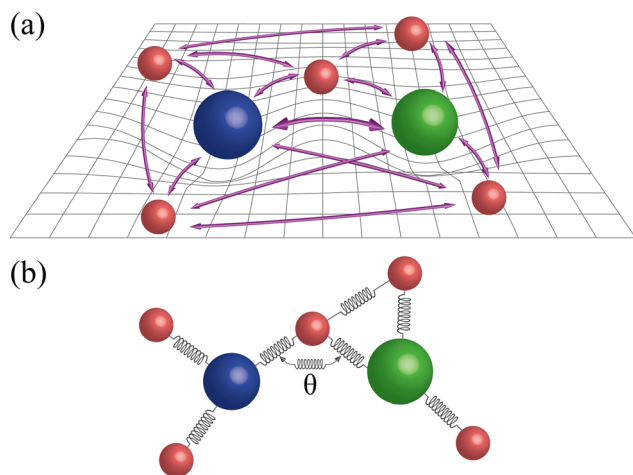*J. Mater. Chem. C*, 2023, **11**, 7595–7602 | 7595

Fig. 1 Schematic representation of (a) two body potential interaction, and (b) bond order dependent potential interaction.

Morse-type pair potential,[22,23] resulting in high accuracy when describing several solid materials, particularly with silicon. The potential has successfully reproduced phenomena such as phase transition from crystalline to amorphous[22] and the dynamic properties of SiO_2.[24] Tersoff's model was further extended to the analytic bond order potential (ABOP),[25] which has been successfully applied to several systems including covalently bonded systems and mixed (ionic and covalent) bond systems.[29–32] The ABOP potential used in this study incorporates Tersoff's formulation of atomic interactions, which takes into account local bond order and angular dependence, and the Brenner parameterization method.[25] Tersoff potentials are widely applied in simulations of sputtering processes for covalent[26,27] and ionic[28] bonding systems, while the Brenner method has been proven to be accurate for simulating film growth *via* atom deposition.[29] By combining these approaches, the ABOP-based potential for IGZO may offer highly precise simulations of the dynamic growth of IGZO films by sputtering, a task that is challenging with conventional two-body potentials. The development of ABOPs for IGZO could aid the study of the material's realistic phases on a mesoscopic scale. However, such potentials do not currently exist, partly due to the vast number of parameters that must be determined for interactions between the quarterly systems. While attempts have been made to parameterize BOPs for ternary systems,[32,33] few studies have been conducted for quarterly systems.

This work presents an ABOP for the IGZO compounds, which was developed by utilizing DFT-calculated atomic binding energies and comparing them to experimental results. The stability of the potential function was assessed through the examination of physical parameters such as X-Ray Diffraction (XRD) data. To validate the newly developed potential, we compared phase transition results from crystalline (c-IGZO) to amorphous (a-IGZO) phases with other MD simulation,[21,34,35] experimental,[36–39] and DFT[40,41] results. The applicability of the ABOP was demonstrated by simulating sputtering processes for dynamic film growth and analyses of the optimal conditions for deposition rates and atomic ratios of the target materials to stabilize the oxygen ratio in sputter-grown IGZO films.

Analytic bond order potential

The ABOP model characterizes three-body interactions in terms of the distance between atoms (r_{ii}) and the angle between them (θ_{iik}), where i, j, and k are indices for the atoms. In a system with n elements, there are $n^3 - n(n - 1)$ possible three-body bonds, excluding equivalent cases. For a binary system composed of two elements (A and B), six sets of parameters are required to describe the interactions (A–A–A, A–A–B, A–B–A, A–B–B, B–A–B, and B–B–B). In the case of a ternary system, there are 21 possible combinations, while for a quarterly system, there are 52. However, the ABOP model only distinguishes between the first and second elements, which reduces the number of combinations to 14. Some of these combinations are already known, and their values can be adopted from the literature to save computation time. Specifically, zinc–zinc, zinc–oxygen, indium–indium, gallium–gallium, and indium–gallium were taken from the pre-developed ABOPs and the Tersoff potential.[42–44] The remaining combinations, which involve metal–oxygen bonds (indium–oxygen and gallium–oxygen) and metal–metal bonds (indium–zinc and gallium–zinc), were parameterized as Table 1 in the following manner.[42,43]

In the ABOP, the total cohesive energy is expressed as a sum over individual binding energies, where the attractive and repulsive interactions are modelled using Morse pair potentials. Specifically, the total energy is given by

$$E = \sum_{i > j} f_C(r_{ij}) \left[V_R(r_{ij}) - \overline{b_{ij}} V_A(r_{ij}) \right] \quad (1)$$

where $f_C(r_{ij})$ is a cutoff function that limits interactions to the nearest neighbours, and $V_R(r_{ij})$ and $V_A(r_{ij})$ are the repulsive and attractive Morse potentials, respectively.

Here, b_{ij} is given as

$$b_{ij} = (1 + \chi_{ij})^{-1/2} \quad (2)$$

where

$$\chi_{ij} = \sum_{k \neq i,j} f_C(r_{ik}) g(\theta_{ijk}) \exp[2\mu_{ik}(r_{ij} - r_{ik})] \quad (3)$$

and

$$g(\theta_{ijk}) = \gamma \left(1 + \frac{c^2}{d^2} - \frac{c^2}{d^2 + (h + \cos\theta)^2} \right) \quad (4)$$

Table 1 ABOP parameters for the IGZO, remaining parameters are in the references[42–44]

Parameter	In–Zn	In–O	Ga–Zn	Ga–O
D_0 (eV)	0.3337	3.2	1.06	3.9
r_0 (Å)	3.4783	1.7	3.2	1.9
S	1.118	1.236	1.766	1.056
β (Å^{-1})	2.291	1.640	1.778	1.659
γ	0.0567	0.05082	0.1150	0.01057
c	1.3590	328.107	242.38	180.28
d	0.9891	11.991	7.2754	9.959
h	0.3310	0.333	0.310	0.316
2μ (Å^{-1})	0.0	0.0	0.0	0.0
R_c (Å)	3.94	2.95	2.95	2.85
D_c (Å)	0.3	0.15	0.2	0.15

7596 | *J. Mater. Chem. C*, 2023, **11**, 7595–7602

This journal is © The Royal Society of Chemistry 2023

As such, b_{ij} provides the local bond-order dependence, whereas $g(\theta ijk)$ gives the angular dependence. With $c = 0$, the term gives the same contribution as the embedded atom method (EAM) potential. By Brenner's direct fitting formalism,[45] the Morse-like attractive and repulsive pair potentials can be parameterized using D_0, the binding energy and r_0, the equilibrium bond length of a dimer such as

$$V_R(r) = \frac{D_0}{S-1} \exp\left(-\beta\sqrt{2S}(r - r_0)\right) \qquad (5)$$

$$V_A(r) = \frac{SD_0}{S-1} \exp\left(-\beta\sqrt{2/S}(r - r_0)\right) \qquad (6)$$

The parameter β can be simply obtained from the ground-state frequency of the dimer molecule. The parameter S is usually adjusted to satisfy the Pauling equation, which connects the equilibrium bond distances and the energy per bond, E_b, as

$$E_b = -D_0 \exp\left[-\beta\sqrt{2S}(r - r_0)\right] \qquad (7)$$

To have a potential widely transferable for all interaction lengths, the calculated data must fulfil the conditions of the Pauling equation. However, to reduce the computational cost, a cut-off function, f_c, is defined to include only the nearest neighbour interactions, which read as

$$f_c(r) = \begin{cases} 1 & r \leq R_c - D_c \\ \frac{1}{2} - \frac{1}{2}\sin\left[\frac{\pi}{2}(r - R_c)/D_c\right] & |r - R_c| \leq D_c \\ 0 & r \geq R_c + D_c \end{cases} \qquad (8)$$

Parameterization by DFT

The ABOP parameters for the desired bonds were found using DFT calculations and compared with experimental observations. Since the cohesive energies predicted by the local density approximation (LDA) tend to be overestimated,[43] the cohesive energies and bond lengths for each structure were scaled down accordingly to match the experimental data. To ensure that the resulting potential is widely transferable and applicable to a broad range of situations, the parameterization process involved as many structures as possible, covering a wide range of bond lengths and the number of interacting atoms. Specifically, the procedure from ref. 42 and 43 was followed, which involved examining rocksalt (NaCl), simple cubic (with basis: CsCl), and zinc blende (ZnS) structures for each dimer.

For the DFT calculations, we used SIESTA DFT suites[46] with the local density approximation (LDA) for the exchange–correlation energy. We employed a carefully chosen cut-off function to calculate only the nearest neighbours of the structures for all examined dimers. To address the issue of local atomic binding, we corrected basis set superposition errors (BSSE) by inserting ghost atoms at the nearest neighbour positions after calculating the cohesive energies of the hypothetical structures.[47] It is worth noting that the differences between with and without the corrections were found to be insignificant.

a. Metal–oxygen bonds

To accurately capture the bond configurations in indium oxide systems, the ABOP parameters were carefully fitted to reproduce the structures of rocksalt, simple cubic, and zinc blende. For realistic bond order dependence, the parameters that produced the best fit to the rocksalt structure were selected, prioritizing the octahedral bond of indium and oxygen atoms in IGZO compounds.[40] Similarly, for the gallium oxide systems, the same fitting procedure was used, but with a focus on achieving the best fit for the zinc blende structure, which better represents the mixed bond nature in the IGZO systems.[40] Given the extensive research on these oxide systems over the years, there is a wealth of literature available on their thermodynamic properties.[48–51] To account for this, the DFT results were scaled down to match the experimental dimer binding energies and equilibrium bond distances. The resulting ABOP parameters are summarized in Table 1.

b. Metal–metal bonds

To model the bond between indium and zinc, DFT calculations were used to obtain the cohesive energies and bond lengths for the rocksalt, simple cubic, and zinc blende structures, which were scaled down by comparison to the experimental dimer binding energies and equilibrium bond lengths.[40] The bond order dependence was parameterized to reproduce the zinc blende structure as accurately as possible. For the gallium–zinc system, the lack of experimental data on dimer binding energies necessitated a different approach. Instead, the results were scaled to best explain the energy per bond length of the rocksalt structures, which were calculated by enthalpy mixing.[52] The equilibrium bond length was obtained from the DFT calculations for an IGZO system,[32] and the bond order was parameterized to represent the zinc blende. It is worth noting that in IGZO systems, the interactions between metals and oxygens play a more decisive role than the interactions between metals. Metals tend to form either octahedral or tetrahedral bonds with oxygen due to the stronger bond between metals and oxygens, and the arrangements of these structures make up the typical IGZO structures. Since metals are usually surrounded by oxygens in these systems, the likelihood of metal–metal bonds is low, and the difference in the interaction parameters between the metal components do not significantly affect the structural properties or the interatomic bond lengths in IGZO simulations.

Molecular dynamics simulations

To assess the performance and capabilities of the developed ABOP for IGZO systems, two types of MD simulations were conducted. The first set of simulations aimed to confirm the validity of the ABOP and involved two steps. In the first step, the stability of the ABOP was evaluated by comparing its results with those obtained using two other commonly used two-body potentials, through room temperature annealing. In the second step, the phase transition from a c-IGZO to an a-IGZO was reproduced using a melt-quenching method. To demonstrate

This journal is © The Royal Society of Chemistry 2023

J. Mater. Chem. C, 2023, **11**, 7595–7602 | **7597**

the capability of the ABOP, the film growth processes of IGZO by sputtering were simulated. These simulations cover the phase transition from particle to solid under mixed pressure and temperature conditions and represent a highly dynamic process of IGZO systems. The successful simulation of sputtering film growth using ABOP would provide strong evidence of broad transferability and its practical application. The MD simulations were conducted using the LAMMPS molecular dynamics package.[53]

a. Stability at room temperature and comparison to two-body potentials

The Buckingham and Morse pair potentials were chosen to be compared to the developed ABOP due to their widespread use in describing interactions in IGZO systems.[21,35] The Buckingham potential, which is a simplified form of Lennard-Jones potential, is mostly developed for describing interactions among gas particles such as helium, neon, and argon.[54] However, with the additional Coulombic interaction term, it can also be used for ionic crystals.[21] The potential is defined as $U_{ij}(r) = A_{ij}\exp(-r/\rho_{ij}) - C_{ij}/r^6$, where r is the distance between the ith and j^{th} atoms. The interaction parameters, A_{ij}, C_{ij}, and ρ_{ij}, need to be determined, and in this work, the parameters reported by Orita $et\ al.$[21] were used, which are summarized in Table 2. Notably, the Buckingham potential used for IGZO completely ignores the interactions between the metal components.

The Morse pair potential consists of a short-range interaction, a long-range Coulomb interaction, and a short-range repulsive term. The short-range repulsive contribution is similar to the $1/r^{12}$ proportional term as in the Lennard-Jones potential. The Morse potential can be written as $U(r) = Z_i Z_j e^2/r + D_{ij}\left[\left\{1 - \exp\left(-a_{ij}(r - r_0)\right)\right\}^2 - 1\right] + C_{ij}/r^{12}$ where r is the distance between the interacting atoms, Z_i is the atomic charge of the ith atom, D_{ij} is the bond dissociation energy, and a_{ij} is the slope of the potential. The energy minimal interatomic distance is represented by r_0. C_{ij} represents the van der Waals repulsion force. In this work, the parameters reported by Buchanan $et\ al.$[35] were used, which are listed in Table 3.

In each MD simulation (with ABOP, Buckingham, and Morse pair), the initial positions of 10 752 atoms were obtained by extending the IGZO crystal configurations from Materials Project,[55] as shown in Fig. 2. For the room temperature annealing simulations, the equilibration of the c-IGZO structure was carried out at 300 K using the isothermal–isobaric (NPT) ensemble conditions with the Nose–Hoover style non-Hamiltonian equation of motion. The simulations were performed for a total of 20 ps with a 0.5 fs timestep.[56,57] The relaxed

Table 2 Buckingham potential parameters for the IGZO

Interaction type	A_{ij} (eV)	ρ (Å)	C_{ij} (eV Å^{12})
In^{3+}–O^{2-}	1293.600	0.331	4.325
Ga^{2+}–O^{2-}	2339.766	0.337	0.000
Zn^{2+}–O^{2-}	600.300	0.274	0.000
O^{2-}–O^{2-}	25.410	0.694	32.320

Table 3 Morse-pair potential parameters for the IGZO

Interaction type	D_{ij} (eV)	a_{ij} (eV Å^{-2})	r_0 (Å)	C_{ij} (eV Å^{12})
In$^{1.8}$–O$^{-1.2}$	0.072975	1.934200	2.824990	3.0
Ga$^{1.8}$–O$^{-1.2}$	0.038263	2.105200	2.668100	0.9
Zn$^{1.2}$–O$^{-1.2}$	0.001221	2.347100	3.149030	1.0
O$^{-1.2}$–O$^{-1.2}$	0.042395	1.379316	3.618701	22.0

structures by the room temperature annealing with three different potentials are depicted in Fig. 2. The ABOP and Morse pair potential resulted in final material densities of 5.91 g cm^{-3} and 6.08 g cm^{-3}, respectively, which agree with the experimental observations of 5.9–6.1 g cm^{-3} of the c-IGZO.[58] In contrast, Buckingham showed a notable difference, with a final density of 4.35 g cm^{-3}.

The crystallinity of the structures obtained by the three different potentials was analysed using virtual X-ray diffraction (XRD) data computed through LAMMPS, with Cu-Kα (1.541838 Å) chosen as the radiation wavelength for comparison with experimental results.[36–38] Fig. 3 displays a comparison between the structure obtained using the ABOP and the experimental results of single-crystal IGZO XRD data.[36–38] The ABOP structure shows excellent agreement with the experimental data, featuring a prominent peak near 30° that corresponds to the strongest peak of (0 0 9) of the single crystal IGZO. Additionally, the agreement is reinforced by the fact that the second and third highest peaks of (0 0 6) and (1 0 12), respectively, also match the experimental data. In contrast, the structure obtained using the Buckingham potential retained its layered structure but deviated from the initial structure substantially as seen in Fig. 2b. The XRD data showed peaks near 40° which is far off from the experimental data.[36–38] The structure obtained from the Morse-pair potential exhibited a loss of crystallinity even after annealing at 300 K, as can be seen from Fig. 2c with no peak at all. This indicates that these two-body potentials are inadequate for realistic MD simulations of IGZO
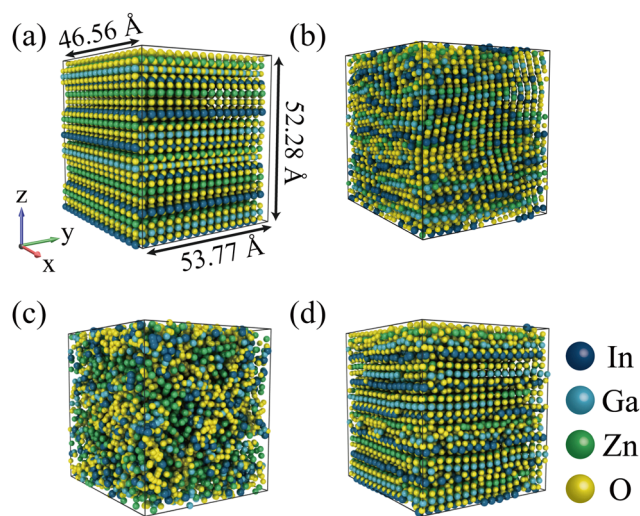

Fig. 2 (a) Initial structure of the c-IGZO structure of 10752 atoms used for the MD simulations, room temperature equilibrated IGZO structure with (b) Buckingham potential, (c) Morse-pair potential, and (d) ABOP.
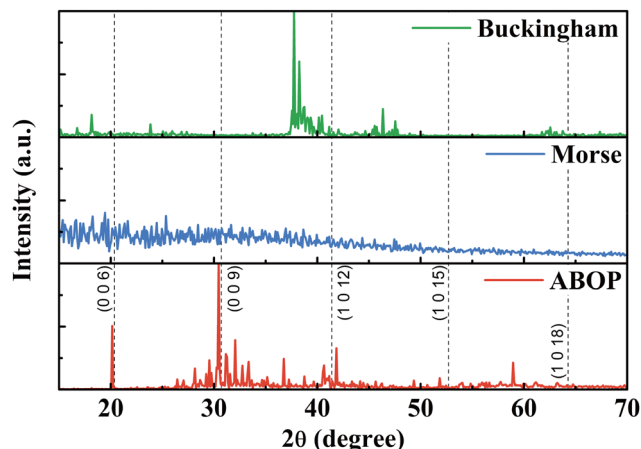
Fig. 3 XRD data of the room temperature equilibrated structures with three different atomic potentials and experimental measurement. Measured XRD peaks of single crystal IGZO are marked as the vertical dashed lines (ref. 38).

systems. Combining the calculated densities and the XRD data, the ABOP demonstrated clear advantages in realistic MD simulations.

b. Phase transition by melt-quenching

To test the newly developed potential's applicability across a wide temperature range, the melt-quenching method was used to form an amorphous phase from a crystalline. The melt-quenching method is commonly used to produce a phase transition and acquire an amorphous phase, as demonstrated for SiO_2 and other materials. The initial system was the same as the room temperature stability simulations, maintained at 300 K for 20 ps. After the initialization, the temperature was elevated to 5000 K under the *NPT* ensemble conditions. Then, the constant temperature was maintained for 40 ps to achieve kinetic equilibrium and ensure a full melting of the system. After complete melting, the system was cooled down to 300 K at 100 K ps^{-1}.

The structural properties after melt-quenching were analysed by radial distribution function (RDF), which shows the correlation between the number of atoms and the interatomic bond lengths. If a structure is crystalline, the RDF displays peaks with regular spacing, and each peak corresponds to the nearest neighbours of the first, second, and so forth. The interatomic distances between metal components in the a-IGZO sample after melt-quenching showed a broader peak around 3.2–3.4 Å, which differs from the sharp peak at 3 Å seen in the room temperature stability test and in c-IGZO. After the melt-quenching, the total volume increased by 7%, from 130905 $Å^3$ to 140773 $Å^3$, and the density decreased from 5.91 g cm^{-3} (c-IGZO) to 5.69 g cm^{-3} (a-IGZO), aligning with density changes seen in a-IGZO and most solids.[40,59]

The metal–oxygen bonds are typically stronger, causing the nearest neighbour of a metal to be an oxygen atom. In RDF data, the first neighbouring peak of each metal represents the metal–oxygen bond. Even after c-IGZO is transformed into a-IGZO through melt-quenching, this does not change, although the location of the first peaks is shifted. In c-IGZO after room temperature annealing, the first neighbouring peak varied based on the metal species, with indium–oxygen bonds near 1.9 Å, gallium–oxygen bonds near 2.2 Å, and zinc–oxygen bonds near 2.1 Å, which is consistent with previous DFT calculations[40,41] and MD simulations.[21,34,35] However, in melt-quenched a-IGZO, the metal–oxygen bonds became consistent at around 2.0 Å for all metal species. In other words, as the material transitions to the amorphous phase, the metal–oxygen bonds become homogenized. In c-IGZO, the metal–metal bonds exhibited long-range order with the second nearest peak being pronounced, followed by the third, fourth, and fifth peaks. However, in a-IGZO, these peaks started to broaden or disappear. The metal–oxygen bonds were similar except for the first neighbouring peak, and the correlations were lost, indicating that the atomic arrangement was randomized at a large scale. This result shows that amorphous phase was successfully obtained using the developed potential.

The RDF data in Fig. 4 indicate an increase in interatomic separations between the metal atoms, indicating that a-IGZO has a lower density than c-IGZO. The lengthening of indium–oxygen bonds is due to their weak binding and higher coordination number. Since indium atoms are larger than those of gallium or zinc, their oxygen binding force is naturally weaker than gallium–oxygen or zinc–oxygen, resulting in a lower attractive potential and allowing the oxygens to get closer to either gallium or zinc. As a result, the gallium– and zinc–oxygen bonds were slightly shortened, while the indium–oxygen bonds were increased. This may require attention in the parameterization of a local bond order potential.

c. IGZO film growth by molecular dynamics

IGZO films are typically grown using sputtering, which involves dynamic phase transitions from particles to solids. To demonstrate the transferability and usefulness of the newly developed ABOP, three sputtering cases were examined using molecular dynamics simulations to investigate the relationship between growth conditions and film properties. The first case involved random deposition at room temperature, where two metal atoms (either indium, gallium, or zinc) were deposited with four oxygen atoms every 2.6 ps. The second case replicated an experimental IGZO growth condition reported by Yabuta *et al.*,[60] with indium, gallium, and zinc atoms introduced every 2.6 ps with four oxygen atoms. The third case simulated sputtering with a high oxygen-content target by increasing the oxygen deposition rate, introducing six oxygen atoms at the same rate instead of four. In each case, a crystalline IGZO substrate consisting of 3024 atoms was placed at the bottom of the simulation domain. The substrate was, firstly, pre-heated at 300 K for 10 ps using the canonical ensemble (NVT) to reach equilibrium. Then, indium, gallium, zinc, and oxygen atoms were introduced (or sputtered) onto the substrate from a distance of 100–120 Å. The kinetic energy of the particles was randomly assigned within a range of 900 to 1100 K, which corresponds to the initial velocities of atoms under real sputtering conditions. The simulations were performed using a timestep of 0.5 fs.
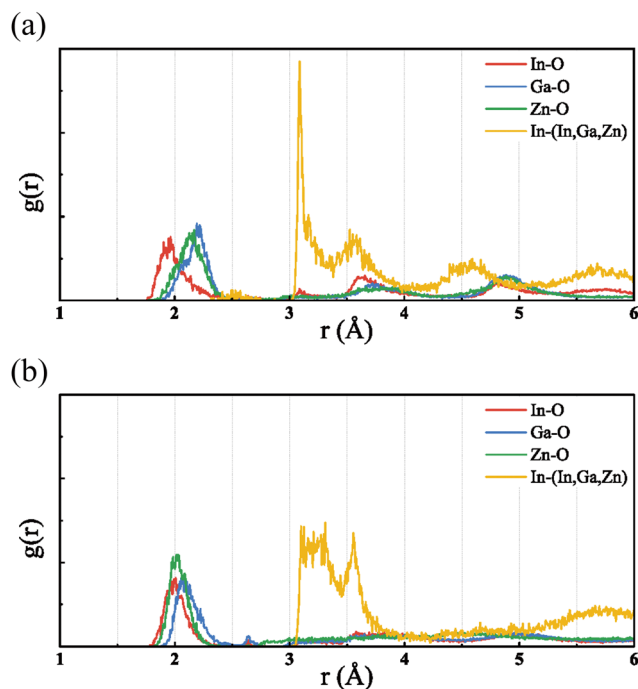
This journal is © The Royal Society of Chemistry 2023

J. Mater. Chem. C, 2023, **11**, 7595–7602 | 7599

Fig. 4 RDF of the (a) room temperature equilibrated structure of c-IGZO, and (b) melt-quenched a-IGZO with the ABOP.

Fig. 5 (a) Deposition rate-controlled sputtered IGZO, (b) random deposition rate sputtered IGZO (void marked in orange), (c) trajectory line of the sputtered atoms at different timesteps in the deposition rate-controlled conditions, (d) trajectory line of the sputtered atoms at different timesteps in the random deposition conditions, and (e) RDF of the deposition rate-controlled conditions.

The rate at which the material is deposited during the film growth has a significant impact on both the growth rate and properties of the resulting film. This is illustrated in Fig. 5, which shows the formation of an a-IGZO film using both rate-controlled (Fig. 5a) and random (Fig. 5b) deposition methods. While both methods produce a-IGZO films, there are drastic differences in their details. In the rate-controlled case, the density of the sputtered IGZO film was 30% higher than that of the random deposition case, with densities of 3.49 g cm^{-3} and 2.68 g cm^{-3}, respectively. The interatomic distances between the metal and oxygen were similar to that of melt-quenched a-IGZO, with near 2 Å in both cases (Fig. 5e). The large difference in densities is due to increased scattering in random depositions. In contrast to the trajectory of atoms in rate-controlled sputtering (Fig. 5c), randomly deposited atoms experience a higher frequency of collisions with the sputtered atoms, resulting in a shorter mean free path, as shown in Fig. 5d. As a consequence, the collided atoms tend to agglomerate before reaching the substrate surface. Once agglomerated, these atoms are adsorbed onto the substrate, forming nanoparticles on the sputter-growth layer. As the deposition process proceeds, the sputtered atoms become attracted to the nanoparticles, ultimately leading to the formation of a blocking layer. This hindered other particles from being sputtered directly to the surface of the substrate, as illustrated in Fig. 5 c and d. At 400 ps, in the rate-controlled case (Fig. 5c), the atoms experience almost no scattering, while in the random deposition case (Fig. 5d), the atoms deposited in the timestep of 400 ps was blocked from being sputtered to lower layers. This resulted in a void marked in Fig. 5b. This blocking layer is experimentally observed as an overhang in sputter-grown films which can be alleviated by lowering the deposition
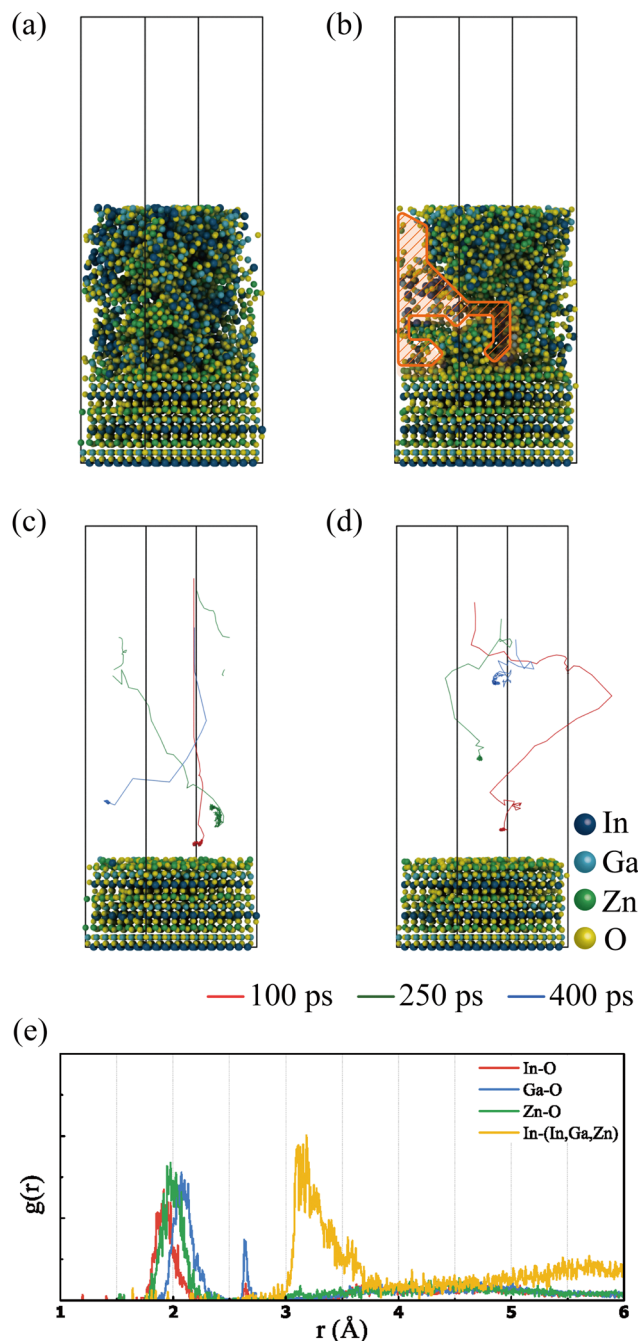
rate.[61,62] The newly developed ABOP model allows for very realistic MD simulations of such phenomena.

To further validate the accuracy of the ABOP model, the atomic ratios of the sputtered film were compared to experimental results. The atomic ratio of the sputtering simulation was In : Ga : Zn = 1.0 : 0.93 : 0.58, which showed excellent agreement with the experimental observation of In : Ga : Zn = 1 : 0.9 : 0.6.[60] However, the sputtered a-IGZO film produced by

7600 | *J. Mater. Chem. C*, 2023, **11**, 7595–7602

This journal is © The Royal Society of Chemistry 2023

the MD simulation had a low oxygen content (In : Ga : Zn : O = 1 : 0.93 : 0.58 : 2.3), which is far from the ideal ratio for $InGaZnO_4$, known to produce the best film quality. The low oxygen ratio indicates the presence of oxygen vacancies in the sputtered a-IGZO film, which can cause negative bias stress (NBS) or negative bias illumination stress (NBIS), leading to device degradation and stability issues.[17] To increase the oxygen content of the sputter-grown IGZO film, a simple approach is to use a high-oxygen-content target. In simulations where the oxygen ratio was increased, the atomic ratio of the sputtered film became closer to the ideal. Using a target with an atomic ratio of In : O = 1 : 6, the sputtered film's oxygen content was increased to In : Ga : Zn : O = 1 : 0.93 : 0.65 : 3.5. Therefore, using a target with an oxygen ratio higher than six times of each metal content is advantageous for obtaining a high-quality IGZO film. Moreover, the simulation results indicate that the developed ABOP for IGZO systems is a versatile tool that can be used to investigate the entire IGZO life-cycle, from film formation to device operation.

Conclusions

To summarize, this study presents the first parameterization of the bond order-dependent atomic potential of IGZO, which has been shown to accurately represent the various phases of IGZO observed in experiments. Notably, the potential is stable under room temperature annealing conditions and can be applied to simulations of sputtering and other processes. This enables the creation of a realistic IGZO bond structure at a mesoscopic scale, which would be difficult to achieve using DFT alone. Furthermore, the potential can be used to investigate the dynamics of crystal formation and optimization of the process conditions for IGZO-based memory and logic devices. By combining DFT calculations with MD simulations, it is possible to obtain electronic and optical properties for realistic IGZO structures. As such, this work opens up new avenues for research that can facilitate the development of IGZO-based technologies.

Conflicts of interest

There are no conflicts to declare.

Acknowledgements

Notes and references

1 C. M. Hsu, W. C. Tzou, C. F. Yang and Y. J. Liou, *Materials*, 2015, **8**, 2769–2781.

2 L. Y. Su, H. Y. Lin, H. K. Lin, S. L. Wang, L. H. Peng and J. J. Huang, *IEEE Electron Device Lett.*, 2011, **32**, 1245–1247.

3 S. Jeong, S. Jang, H. Han, H. Kim and C. Choi, *J. Alloys Compd.*, 2021, **888**, 161440.

4 W. Xu, L. Hu, C. Zhao, L. Zhang, D. Zhu, P. Cao, W. Liu, S. Han, X. Liu, F. Jia, Y. Zeng and Y. Lu, *Appl. Surf. Sci.*, 2018, **455**, 554–560.

5 J. S. Park, W. J. Maeng, H. S. Kim and J. S. Park, *Thin Solid Films*, 2012, **520**, 1679–1693.

6 T. Kamiya, K. Nomura and H. Hosono, *Sci. Technol. Adv. Mater.*, 2010, **11**, 044305.

7 F. Mo, Y. Tagawa, C. Jin, M. J. Ahn, T. Saraya, T. Hiramoto and M. Kobayashi, *IEEE J. Electron Devices Soc.*, 2020, **8**, 717–723.

8 A. Chasin, L. Zhang, A. Bhoolokam, M. Nag, S. Steudel, B. Govoreanu, G. Gielen and P. Heremans, *IEEE Electron Device Lett.*, 2014, **35**, 642–644.

9 H. Luo, P. Wellenius, L. Lunardi and J. F. Muth, *IEEE Electron Device Lett.*, 2012, **33**, 673–675.

10 B. D. Yang, *ETRI J.*, 2013, **35**, 610–616.

11 W. Assenmacher, G. Schnakenburg, Y. Michiue, Y. Kanke, N. Kimizuka and W. Mader, *J. Solid State Chem.*, 2014, **215**, 176–183.

12 J. Sheng, T. H. Hong, H.-M. Lee, K. R. Kim, M. Sasase, J. Kim, H. Hosono and J. S. Park, *ACS Appl. Mater. Interfaces*, 2019, **11**, 40300–40309.

13 A. Olziersky, P. Barquinha, A. Vilà, C. Magaña, E. Fortunato, J. R. Morante and R. Martins, *Mater. Chem. Phys.*, 2011, **131**, 512–518.

14 K. Tsutsui, D. Matsubayashi, N. Ishihara, T. Takasu, S. Matsuda and S. Yamazaki, *Appl. Phys. Lett.*, 2015, **107**, 262104.

15 Y. Yamada, D. Matsubayashi, S. Matsuda, Y. Sato, M. Ota, D. Ito, M. Tsubuku, M. Takahashi, T. Hirohashi, M. Sakakura and S. Yamazaki, *Jpn. J. Appl. Phys.*, 2014, **53**, 091102.

16 Y. Jegal, A. H. Kulahlioglu, C. K. Baek and B. D. Kong, *IEEE Electron Device Lett.*, 2020, **41**, 872–875.

17 A. de Jamblinne de Meux, A. Bhoolokam, G. Pourtois, J. Genoe and P. Heremans, *Phys. Status Solidi A*, 2017, **214**, 1600889.

18 H. Omura, H. Kumomi, K. Nomura, T. Kamiya, M. Hirano and H. Hosono, *J. Appl. Phys.*, 2009, **105**, 093712.

19 G. C. Abell, *Phys. Rev. B: Condens. Matter Mater. Phys.*, 1985, **31**, 6184–6196.

20 F. H. Stillinger and T. A. Weber, *Phys. Rev. B: Condens. Matter Mater. Phys.*, 1985, **31**, 5262–5271.

21 M. Orita, H. Tanji, M. Mizuno, H. Adachi and I. Tanaka, *Phys. Rev. B: Condens. Matter Mater. Phys.*, 2000, **61**, 1811–1816.

22 J. Tersoff, *Phys. Rev. B: Condens. Matter Mater. Phys.*, 1988, **37**, 6991–7000.

23 J. Tersoff, *Phys. Rev. B: Condens. Matter Mater. Phys.*, 1989, **39**, 5566–5568.

24 S. Munetoh, T. Motooka, K. Moriguchi and A. Shintani, *Comput. Mater. Sci.*, 2007, **39**, 334–339.

This journal is © The Royal Society of Chemistry 2023

J. Mater. Chem. C, 2023, **11**, 7595–7602 | **7601**

25 K. Albe, K. Nordlund, J. Nord and A. Kuronen, *Phys. Rev. B: Condens. Matter Mater. Phys.*, 2002, **66**, 035205.

26 A. P. Prskalo, S. Schmauder, C. Ziebert, J. Ye and S. Ulrich, *Surf. Coat. Technol.*, 2010, **204**, 2081–2084.

27 J. Tanaka, C. F. Abrams and D. B. Graves, *J. Vac. Sci. Technol., A*, 2000, **18**, 938–945.

28 L. Zhang, H. Yan, G. Zhu, S. Liu and Z. Gan, *R. Soc. Open Sci.*, 2018, **5**, 180629.

29 D. W. Brenner, *Phys. Rev. B: Condens. Matter Mater. Phys.*, 1990, **42**, 9458–9471.

30 K. Albe, K. Nordlund and R. S. Averback, *Phys. Rev. B: Condens. Matter Mater. Phys.*, 2002, **65**, 195124.

31 J. Nord, K. Albe, P. Erhart and K. Nordlund, *J. Phys.: Condens. Matter*, 2003, **15**, 5649–5662.

32 N. Juslin, P. Erhart, P. Träskelin, J. Nord, K. O. Henriksson, K. Nordlund, E. Salonen and K. Albe, *J. Appl. Phys.*, 2005, **98**, 123520.

33 K. Matsunaga, C. Fisher and H. Matsubara, *Jpn. J. Appl. Phys.*, 2000, **39**, L48.

34 K. Ide, K. Nomura, H. Hiramatsu, T. Kamiya and H. Hosono, *J. Appl. Phys.*, 2012, **111**, 073513.

35 J. C. Buchanan, D. B. Fast, B. E. Hanken, T. J. Mustard, G. Laurita, T. H. Chiang, D. A. Keszler, M. A. Subramanian, J. F. Wager, M. R. Dolgos, J. R. Rustad and P. H.-Y. Cheong, *Dalton Trans.*, 2017, **46**, 15311–15316.

36 D. M. Lynch, B. Zhu, B. D. Levin, D. A. Muller, D. G. Ast, R. G. Greene and M. O. Thompson, *Appl. Phys. Lett.*, 2014, **105**, 262103.

37 X. Wang, Z. Shen, J. Li and S. Wu, *Membranes*, 2021, **11**, 134.

38 Y. Tanaka, K. Wada, Y. Kobayashi, T. Fujii, S. J. Denholme, R. Sekine, N. Kase, N. Kimizuka and N. Miyakawa, *CrystEngComm*, 2019, **21**, 2985–2993.

39 K. Nomura, T. Kamiya, H. Ohta, T. Uruga, M. Hirano and H. Hosono, *Phys. Rev. B: Condens. Matter Mater. Phys.*, 2007, **75**, 035212.

40 T. Kamiya, K. Nomura and H. Hosono, *J. Disp. Technol.*, 2009, **5**, 273–288.

41 T. Nakayama, M. Takahashi, T. Kanagawa, T. Obonai, K. Okazaki and S. Yamazaki, *ECS Trans.*, 2019, **90**, 21–33.

42 P. Erhart, N. Juslin, O. Goy, K. Nordlund, R. Müller and K. Albe, *J. Phys.: Condens. Matter*, 2006, **18**, 6585–6605.

43 T. Hammerschmidt, P. Kratzer and M. Scheffler, *Phys. Rev. B: Condens. Matter Mater. Phys.*, 2008, **77**, 235303.

44 Y. Nishidate and G. P. Nikishkov, *Comput. Model. Eng. Sci.*, 2008, **26**, 91.

45 D. W. Brenner, *Phys. Rev. B: Condens. Matter Mater. Phys.*, 1990, **42**, 9458–9471.

46 J. M. Soler, E. Artacho, J. D. Gale, A. García, J. Junquera, P. Ordejón and D. Sánchez-Portal, *J. Phys.: Condens. Matter*, 2002, **14**, 2745–2779.

47 P. D. Haynes, C.-K. Skylaris, A. A. Mostofi and M. C. Payne, *Chem. Phys. Lett.*, 2006, **422**, 345–349.

48 K.-P. Huber and G. Herzberg, *Molecular spectra and molecular structure, iv: Constants of diatomic molecules*, Van Nostrand Reinhold, New York, 1979.

49 W. J. Svirbely and S. M. Read, *J. Phys. Chem.*, 1962, **66**, 658–662.

50 D. R. Hagleitner, M. Menhart, P. Jacobson, S. Blomberg, K. Schulte, E. Lundgren and U. Diebold, *Phys. Rev. B: Condens. Matter Mater. Phys.*, 2012, **85**, 115441.

51 S. Stepanov, V. Nikolaev, V. Bougrov and A. Romanov, *Rev. Adv. Mater. Sci.*, 2016, **44**, 63–86.

52 E. C. Do, Y. H. Shin and B. J. Lee, *J. Phys.: Condens. Matter*, 2009, **21**, 325801.

53 A. P. Thompson, H. M. Aktulga, R. Berger, D. S. Bolintineanu, W. M. Brown, P. S. Crozier, P. J. in 't Veld, A. Kohlmeyer, S. G. Moore, T. D. Nguyen, R. Shan, M. J. Stevens, J. Tranchida, C. Trott and S. J. Plimpton, *Comput. Phys. Commun.*, 2022, **271**, 108171.

54 R. A. Buckingham, *Proc. R. Soc. London, Ser. A*, 1938, **168**, 264–283.

55 A. Jain, S. P. Ong, G. Hautier, W. Chen, W. D. Richards, S. Dacek, S. Cholia, D. Gunter, D. Skinner, G. Ceder and K. A. Persson, *APL, Materials*, 2013, **1**, 011002.

56 S. Nosé, *J. Chem. Phys.*, 1984, **81**, 511–519.

57 W. G. Hoover, *Phys. Rev. A: At., Mol., Opt. Phys.*, 1985, **31**, 1695–1697.

58 S. Yamazaki, *ECS Trans.*, 2014, **64**, 155.

59 X. Y. Cui, S. P. Ringer, G. Wang and Z. H. Stachurski, *J. Chem. Phys.*, 2019, **151**, 194506.

60 H. Yabuta, M. Sano, K. Abe, T. Aiba, T. Den, H. Kumomi, K. Nomura, T. Kamiya and H. Hosono, *Appl. Phys. Lett.*, 2006, **89**, 112123.

61 S. Swann, *Phys. Technol.*, 1988, **19**, 67.

62 D. S. Taylor, M. K. Jain and T. S. Cale, *J. Vac. Sci. Technol., A*, 1998, **16**(5), 3123–3126.

7602 | *J. Mater. Chem. C*, 2023, **11**, 7595–7602

This journal is © The Royal Society of Chemistry 2023